Materials Science & Engineering A 615 (2014) 283–295

Contents lists available at ScienceDirect

Materials Science & Engineering A

journal homepage: www.elsevier.com/locate/msea

Investigation and modeling of the anomalous yield point phenomenon in pure tantalum

D. Colas [a,b,c], E. Finot [a], S. Flouriot [b], S. Forest [c], M. Mazière [c,*], T. Paris [b]

[a] Laboratoire Interdisciplinaire Carnot de Bourgogne, UMR 5209 CNRS, Université de Bourgogne, 9 avenue Alain Savary, BP 17870, 21078 Dijon Cedex, France
[b] CEA Valduc, 21120 Is-sur-Tille, France
[c] Mines ParisTech, Centre des Matériaux, CNRS, UMR 7633, BP 87, 91003 Evry Cedex, France

ARTICLE INFO

Article history:
Received 22 April 2014
Accepted 10 July 2014
Available online 29 July 2014

Keywords:
Tantalum
Band propagation
Strain localization
Static strain aging
Infrared thermography

ABSTRACT

The monotonic and cyclic behavior of commercially pure tantalum has been investigated at room temperature, in order to capture and understand the occurrence of the anomalous yield point phenomenon. Interrupted tests have been performed, with strain reversals (tensile or compressive loading) after an aging period. The stress drop is attributed to the interactions between dislocations and solute atoms (oxygen) and its macroscopic occurrence is not systematically observed. InfraRed Thermography (IRT) measurements supported by Scanning Electron Microscopy (SEM) pictures of the polished gauge length of a specimen during an interrupted tensile test reveal the nucleation and propagation of a strain localization band.

The KEMC (Kubin–Estrin–McCormick) phenomenological model accounting for strain aging has been identified for several loadings and strain rates at room temperature. Simulations on full specimen using the KEMC model do not show strain localization, because of the competition between viscosity and strain localization. However, a slight misalignment of the sample can promote strain localization.

1. Introduction

Tantalum is a refractory material used in several industries such as nuclear, capacitors, lighting, biomedical and chemical processing. In the past few decades, many researches on tantalum behavior have been carried out, but only few were focused on low strain rates [1–6]. Most of them are dedicated to large strains and/or large strain rates [7–14]. Moreover, only few studies at room temperature are available. Conversely, they have been performed at very low temperatures for the intrinsic behavior knowledge [19,47], or at high temperatures for dynamic strain aging studies [4,35]. Furthermore, some fundamental works have been done on tantalum single crystals of various orientations both in tension and compression [15,16].

In many metallic alloys, the transition from elastic to plastic regimes is characterized by a material instability known as the Lüders phenomenon (mainly for steels) [21–27]. In that case, a sharp yield point is followed by a Lüders stress plateau, associated with the propagation of a localized deformation band through the gauge length. The band usually nucleates at one grip, leading to a stress drop. The plastically strained area then spreads along the sample. See [21] and references quoted therein for more details.

In the literature, some other materials exhibit an anomalous yield point with different features, such as niobium, which also has a BCC lattice structure [17]. An anomalous yield point is reported for this material, but without band propagation. Zirconium has an HCP lattice structure and presents a small stress drop associated to yielding, but its shape is very different. The important role of solute atoms such as oxygen on the strain aging has been extensively studied in zirconium, but no band propagation has been reported [28–31]. Commercially pure titanium has also been considered, but the stress drop associated to yielding is very small, without macroscopic band propagation [32–34]. The anomalous yield point phenomenon in tantalum has never been investigated in detail, although if it has been evidenced on several experimental curves [1–3,6,17–20].

The origin of the anomalous yield point lies in the presence of the solute atoms interacting with dislocations. In the literature, two main theories about the pinning mechanisms exist: the first associates the stress drop to the so-called “Snoek ordering” of interstitial atoms in the crystal lattice because of the stress fields around dislocations, creating a tetragonal distortion of the BCC lattice structure [1,17,19,35,36]. The reordering and “jumping” of solute atoms from a barrier to another in order to reduce the total energy of the system require an additional stress leading to the macroscopic stress peak and stress drop.

Alternatively, the sharp yield phenomenon can be due to the long range drift of interstitial atoms to form the so-called “atmospheres”

* Corresponding author. Tel.: +33 160763078; fax: +33 160763150.
E-mail address: matthieu.maziere@mines-paristech.fr (M. Mazière).

http://dx.doi.org/10.1016/j.msea.2014.07.028
0921-5093/

[9,13,19,37–42]. In that case, the dislocations pinning by solute atoms requires an additional stress for their motion. The stress drop is the macroscopic expression of the unpinning process. SEM and TEM observations of this phenomenon have been performed, showing the dislocation structure formation during deformation [4,5,7,8,13,20,43]. The appearance of slip lines at the surface in the region of the localization band has been observed for steels [23,44], but never for pure tantalum.

The dominating effects of oxygen, carbon and nitrogen have been widely studied in the case of tantalum [4,19,36,45–48]. Oxygen seems to be the principal element involved in the anomalous sharp yield point. Moreover, oxygen has the highest diffusivity coefficient compared to nitrogen and carbon [35,19,48]. On the other hand, interstitial content also has an impact on the failure mode by embrittling the material [4,24,25,49].

Some mechanical models have been proposed in the literature for tantalum. They are based on the combination of isotropic and kinematic non-linear hardenings [18]. Some physical parameters are often used, such as the dislocation density and its evolution, mainly for large strains and high strain-rates applications [8,9,12,14,18]. Similar models have been used for the computation of the dynamic expansion of a spherical shell [11]. Those models are able to capture the large strain behavior, as well as shearing and impact tests [10]. Some models have been used in order to compute processes such as welding [50] or hydro-forming [53]. The texture evolution using a polycrystalline model has also been investigated [51,52].

Among them, some attempts have been carried out in order to account for static strain aging [43,50]. The stress peak has been computed by adding an isotropic softening term, depending on the accumulated plastic strain. Those attempts however are not sufficient for an accurate modeling because of their purely phenomenological formulation.

In our case, the origin of the anomalous yield point phenomenon is attributed to oxygen-dislocation interactions, and its macroscopic (and mesoscopic) manifestation is rather well known. Thus, the aim of the present paper is to propose a macroscopic characterization, with a simple but efficient modeling accounting for the anomalous yield point phenomenon. The effects of the experimental setup on the anomalous yield point and on the thermal fields through several numerical will be demonstrated, giving a new insight on the phenomenon. A macroscopic approach is adopted, for both numerical and experimental approaches. A combination of mechanical tests, InfraRed Thermography (IRT) and SEM images is used for the characterization.

In Section 2, several mechanical tests performed at room temperature for strain rates from $\dot{\varepsilon} = 10^{-4}\ s^{-1}$ to $10^{-2}\ s^{-1}$ are presented. First, tensile tests have been performed, coupled to IRT. Then, strain controlled cyclic tests have been carried out for several strain amplitudes, giving further information about the behavior at room temperature. Moreover, specific tests called "strain reversal", inspired by Orowan have been carried out [21,68,76]. It consists of interrupted mechanical tests, where the sample is unloaded after straining and aged 1 day at 100 °C. The sample is then reloaded, leading to different macroscopic responses depending on the strain direction chosen. Some in situ mesoscopic analysis using SEM imaging is reported that can be combined to IRT measurements and to the macroscopical response for the understanding of the consequences of the unpinning processes.

In Section 3, a macroscopic model has been developed that takes into account the anomalous yield point phenomenon and the strain rate sensitivity. This model is based on the so-called "KEMC" model from Kubin, Estrin and McCormick [56–60]. The stress drop is computed using an additional internal variable t_a representing the time left to interstitial atoms to diffuse along dislocations. The proper alignment of the sample plays an important role that changes drastically the strain and strain rate fields of the gauge length, resulting from the competition between viscosity and localization. This may explain the limited reproducibility of the anomalous yield point observed in the literature.

Table 1
Impurity analysis of tantalum in ppm.

Element	C	N	O	H
ppm (weight)	10	< 10	19	6

2. Experimental results

2.1. Material and experimental methods

2.1.1. Material

The material studied is a commercially pure tantalum (99.95 wt %) coming from Cabot Performance Materials (USA). The sheet used has been recrystallized during 2 h between 1000 and 1200 °C and 10^{-4}–10^{-5} mbar. Tantalum has a BCC lattice structure with a composition in solute atoms reported in Table 1.

After recrystallization, the mean grain size is close to 100 μm and the initial dislocation density is rather high, between $\rho_d \approx 10^{13}\ m^{-2}$ and $\rho_d \approx 10^{14}\ m^{-2}$ [5,14,43,61,62].

A simple computation shows that a value of 5.5 ppm is sufficient to saturate all the dislocations. The initial dislocation density is $10^{14}\ m^{-2}$, the lattice parameter of $a = 3.2959$ Å, with a molar volume of $10.85 \times 10^{-6}\ m^3\ mol^{-1}$ or an atomic volume of 18.0168 Å^3.

We assume that all the atomic sites of the $\rho = 10^{14}\ m\ m^{-3}$ dislocations (1 dislocation every 100 nm if they are uniformly spaced) are filled. The atom number per meter of dislocation is $\frac{10^{10}}{3.2959} = 3.03 \times 10^9$ atoms. The number of solute atoms per m^3 for a dislocation density of $10^{14}\ m\ m^{-3}$ is $3.03 \times 10^9 \times 10^{14} = 3.03 \times 10^{23}$.

Finally, the number of atoms per m^3 (or 10^{30} Å^3) is $\frac{10^{30}}{18.0168} = 5.55 \times 10^{28}$. The number of solute atoms required to saturate $10^{14}\ m^{-2}$ dislocations is $\frac{3.03 \times 10^{23}}{5.55 \times 10^{28}} = 5.5 \times 10^{-6}$ or 5.5 ppm (atomic) or ≈0.5 ppm (weight).

2.1.2. Specimen design

Two geometries have been used: thin flat samples for monotonic tensile tests, IRT and SEM data acquisition, and thicker flat samples for cyclic tension – compression loading, in order to get rid of potential buckling (Fig. 1, resp. (a) and (b)).

2.1.3. Tests machines

Two testing machines were used for the test campaign. Tensile tests were conducted using an electro-mechanical Zwick 100 kN testing machine, with a 38.5 kN/mm stiffness. For cyclic and strain reversal loadings, a servo-hydraulic Instron 8800 machine was used, with an higher stiffness of 79.3 kN/mm. Loading of the specimen was applied quasi-statically by prescribing a constant velocity for the stroke of the actuator in the testing device. Average strain over the gauge length is measured using an extensometer. The machine stiffness is known to play a significant role in the manifestation of strain aging phenomena [78].

2.1.4. IR camera

The camera used for the thermal field measurements is a FLIR SC 7500, with a spatial resolution of 320 × 256 px. (≈100 μm/px.) and a sensitivity of 20 mK. Working with relative images instead of

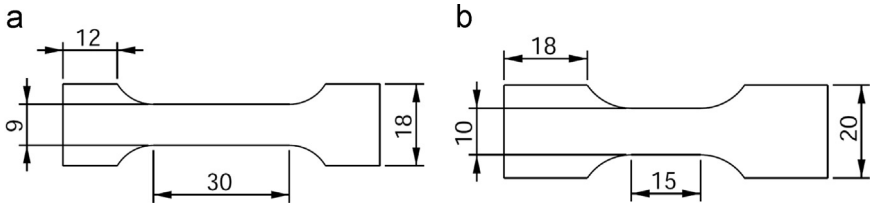

Fig. 1. (a) Tensile test sample geometry, 2.5 mm thick, (b) cyclic and strain reversal tests sample geometry, 8 mm thick.

absolute ones is the better way to strongly increase measurement precision up to 10 mK, by subtracting the first frame (permanent noise). The apparent temperature of the sample is calculated using Planck's law that connects the radiation of a body with its temperature. In order to improve the surface emissivity up to 0.96, ensure its stability and measure the sample's real temperature, specimen's surface has been painted in black. For more details about this technique, see [63–65].

2.2. Mechanical response at room temperature

2.2.1. Tensile tests

Fig. 2 shows the strain–stress response at room temperature for several strain rates. The upper yield point is the maximum stress following the linear elastic regime where the deformation is expected to be still homogeneous. At room temperature, the anomalous yield point phenomenon is associated to a strong strain rate sensitivity (40 MPa per decade), a high ductility and a monotonic strain hardening roughly independent of the strain rate (for low strain rates without thermal softening). Our study will focus on the first percents of strain, where the stress drop associated to yielding is predominant (Fig. 2(b)).

The shape of the anomalous yield point is substantially different from other materials. In the case of steels, the stress drop is associated to the nucleation (usually at one grip) and propagation of a plastic deformation band through the sample [21,26,27,55]. In our case, the band propagation seems to be more diffuse (as we will see below with the IRT measurements), coupled with the strong strain rate dependence of the shape of the stress drop on the macroscopic curves.

2.2.2. Cyclic tests

Several cyclic tests ware carried out, for strain amplitudes ranging from $\pm 0.18\%$ to $\pm 0.5\%$ at $\dot{\varepsilon} = 10^{-3}\,s^{-1}$ (Fig. 3). If the strain amplitude is small ($\pm 0.18\%$, Fig. 3(a)), a slight small cyclic softening is observed. The first unloading has been performed at the upper yield point, thus the softening associated to the stress drop keeps going during the first compression. The shape of the hysteresis loop is sharp, with a strong Baushinger effect. For the intermediate strain amplitude ($\pm 0.25\%$, Fig. 3(b)), no cyclic hardening is observed. The first compression branch has a particular shape, showing a bump and a slight softening, possibly due to an ongoing band propagation through the gauge length. In the last case studied ($\pm 0.5\%$, Fig. 3(c)), a strong cyclic hardening (more than 50 MPa) is observed. The first unloading happens after the end of the stress drop and the hysteresis loop has a flatter shape. The cyclic hardening/softening behavior depending on the strain amplitude is summarized in Fig. 3(d).

Cyclic tests emphasize the existence of a link between the strain amplitude and the cyclic hardening or softening, in agreement with the literature on BCC metals [54]. This specific behavior has been related to the different dislocations' families involved in the strain accommodation as a function of strain amplitude.

For small strain amplitudes, dislocation density is almost constant, with long segments of screw dislocations having a weak mobility. Thus, the major part of the cyclic strain is adapted by edge dislocations. Dislocation interactions are weak, leading to a small multiplication. This leads to an insignificant hardening at the macro scale. This combines with the softening associated to the unpinning process of dislocation from solute atoms.

For larger strain amplitudes, other dislocations families become active: an intense screw dislocations multiplication is observed. Moreover, edge dislocations clusters form mediated by cross slip. Thus a dislocations densification takes place in the bulk and a cyclic hardening is macroscopically observed [66,54,67]. In the same time, the unpinning process is over at the first unloading and consequently does not affect the cyclic hardening.

2.2.3. Strain reversal with aging

Strain reversal tests are a robust way to evidence strain aging effects leading to the anomalous yielding phenomenon. Those tests have been performed firstly by Orowan on steels in the 1960s and published recently by Elliot [68]. These tests investigate the influence of the straining direction before and after an aging period. The same kind of tests was performed on tantalum in the present work and is presented in Fig. 4. Three successive sequences of tensile loadings are carried out, and finally a compressive loading is carried out.

Between each loading sequence, the sample is unmounted and aged 1 day at 100 °C before a new loading sequence is started. Tensile and compressive tests have been performed using an anti-buckling system having a thin PTFE interface. The anomalous yield point is systematically observed for any loading before and after aging. The same sequential tests have been performed without anti-buckling systems, and the results show the same tendency. The same test has been carried out with shorter heat treatment (2 h). In that case, the stress drop is not systematically observed.

As a conclusion, the anomalous yield phenomenon is systematically observed if the aging time is sufficient (1 day at 100 °C). A strong softening is noticeable after the sharp yield point (roughly 50 MPa, i.e. 20% of the upper yield point). Its shape is less sharp than in the case of steels and is combined with a large strain rate sensitivity. In the following, the material is considered aged enough to produce a sharp yield point systematically, as we can see in Fig. 4.

2.3. Thermal fields measurements

Some monotonic tensile experiments have been carried out together with thermal fields measurements for a better understanding of the underlying mechanisms leading to the anomalous yield point phenomenon. This kind of measures is very sensitive to experimental conditions, to the specimen's geometry, to the alignment in the grips and to testing machine settings.

A weak overheating is observed in Fig. 5 during the tensile tests (coupled with a high thermal conductivity compared to other metals): only 0.5 K of temperature increase in the yield point domain. Moreover, the heating rate is low, pointing out a weak plastic strain localization (weak dissipation).

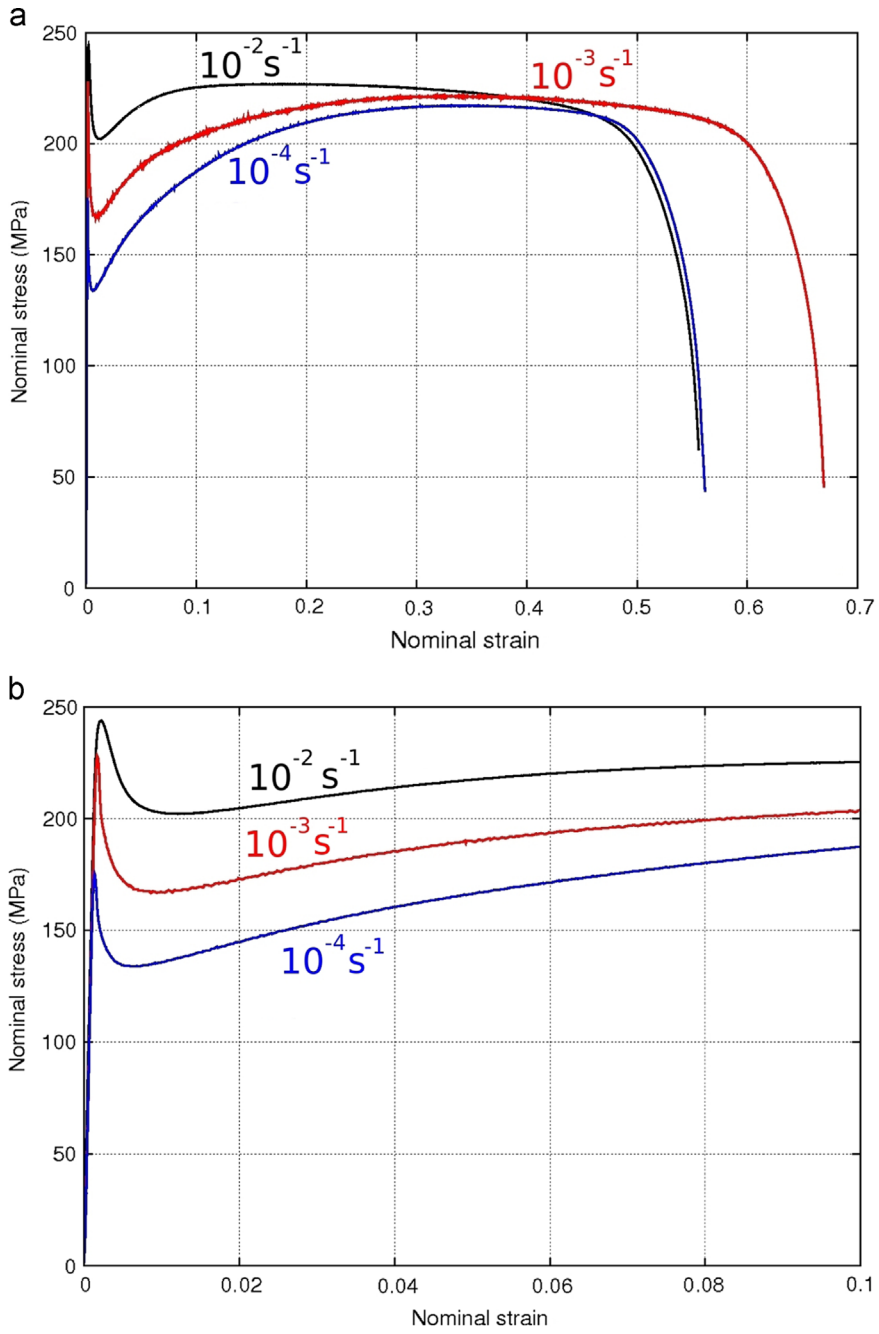

Fig. 2. Tensile test at room temperature for several strain rates from $\dot{\varepsilon} = 10^{-4}\ s^{-1}$ to $10^{-2}\ s^{-1}$. (a) Complete tensile test, (b) closeup on the first ten percents.

The first experiment (sample 1) (Fig. 5, left) shows a visible band nucleation, while the second one (sample 2, right) appears much more diffuse. The propagation of a band is then similar in both cases. The low temperature increase indicates a moderate localization inside the band.

It is interesting to notice that the stress drop of sample 2 in Fig. 6 is smaller, smoother and wider than sample's 1 stress drop. In that case, the localization associated to the band propagation is more diffuse and no clear band appears on the infrared measurement.

2.4. SEM data acquisitions of slip line development

A tensile test carried out at room temperature and $\dot{\varepsilon} = 10^{-3}\ s^{-1}$ has been interrupted four times at different macroscopic plastic strains (0.15%, 0.25%, 0.8% and 1.7%). At each step, the load has been decreased to zero in order to observe the specimen ex situ in a SEM. The macroscopic strain–stress response is shown in Fig. 7. SEM data of the undeformed sample show a significant mosaicity, mainly due to a partial recrystallization and a surface hardening induced by sample's machining, as already observed on tantalum [62] (cf. Fig. 8).

The specimen was first unloaded at the beginning of the stress drop (at 0.15% of macroscopic plastic strain). A macroscopic localization band was visible on the polished surface of the sample, near a grip (Fig. 8). SEM pictures of this region show many slip lines inside the grains, whereas in the center region nothing has occurred. This localization depends both on grain orientation and on grain cluster effect.

During the next loadings, the macroscopic band moves forward and finally reaches the other fillet. Two other SEM pictures of some different regions clearly show the propagation of the band after 0.25% and 0.8% of macroscopic plastic strain (resp. Figs. 9 and 10).

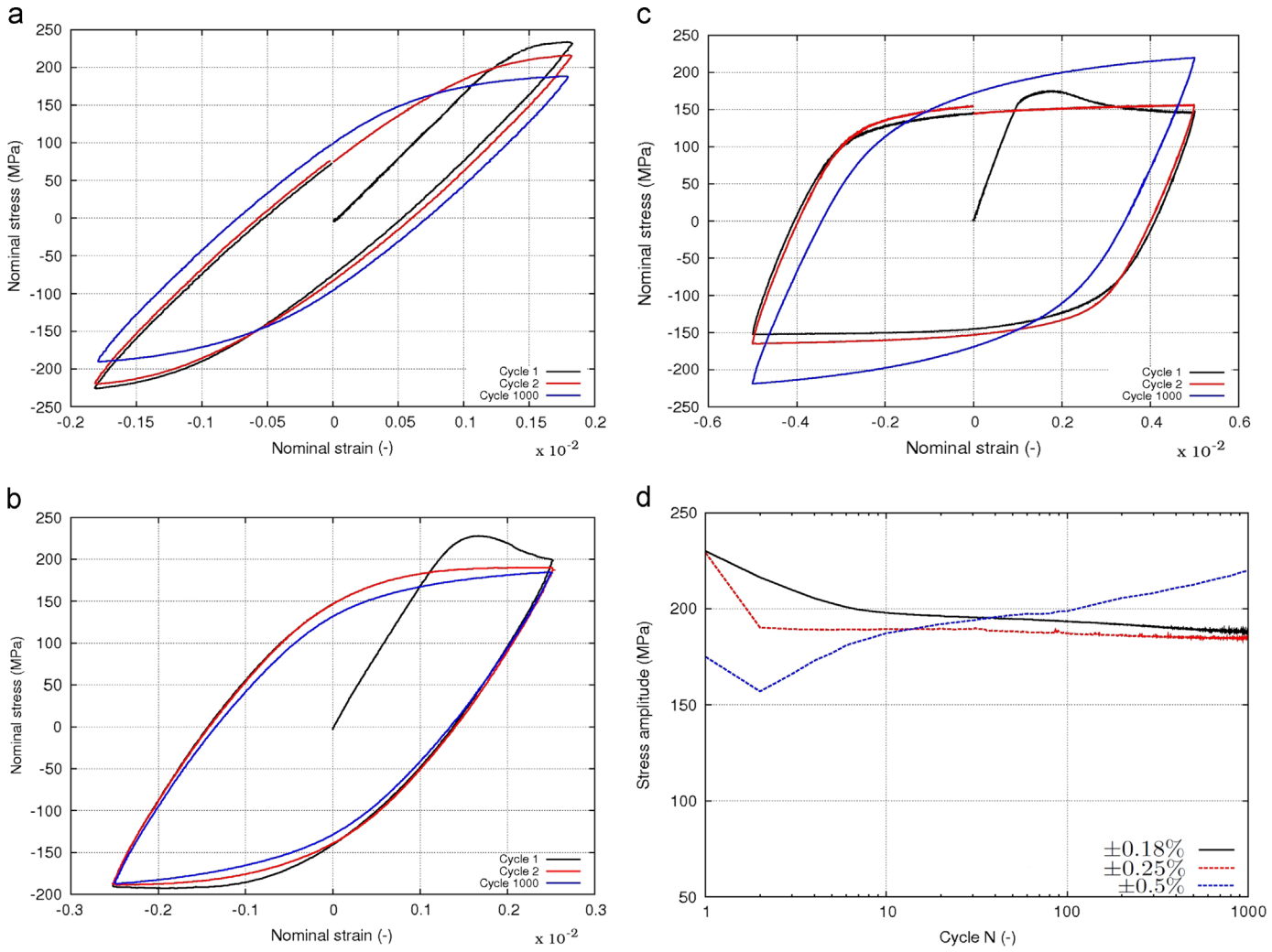

Fig. 3. Hysteresis loop for several strain amplitudes: (a) $\pm 0.18\%$, (b) $\pm 0.25\%$, (c) $\pm 0.5\%$ at $\dot{\varepsilon} = 10^{-3}\ s^{-1}$, (d) global cyclic hardening behavior.

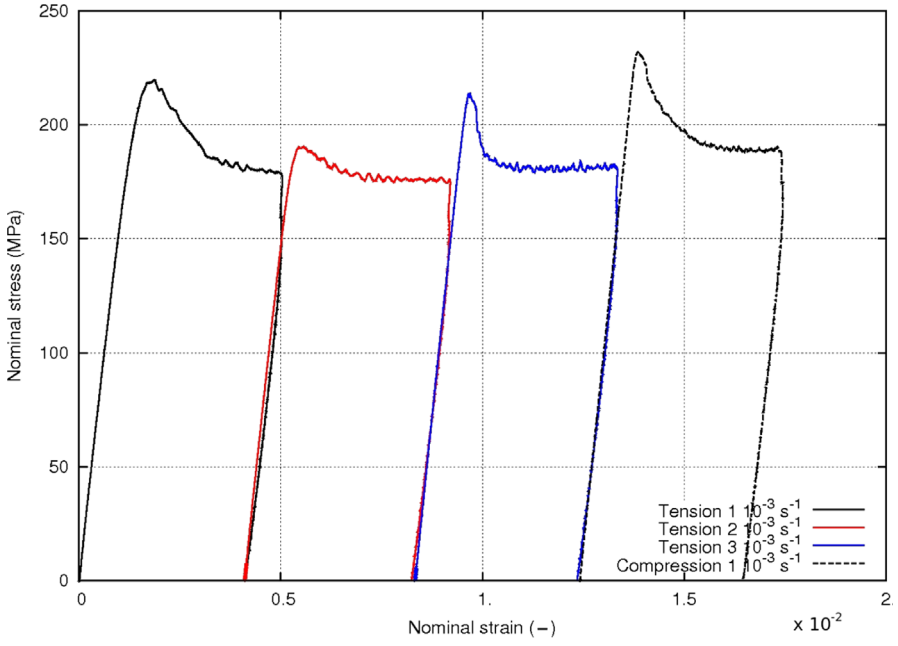

Fig. 4. Strain reversal after aging at room temperature and $\dot{\varepsilon} = 10^{-3}\ s^{-1}$. Serrations visible on the curves are due to the machine's servo-control. The compression part has been reversed in the positive strain domain to follow Orowan's description.

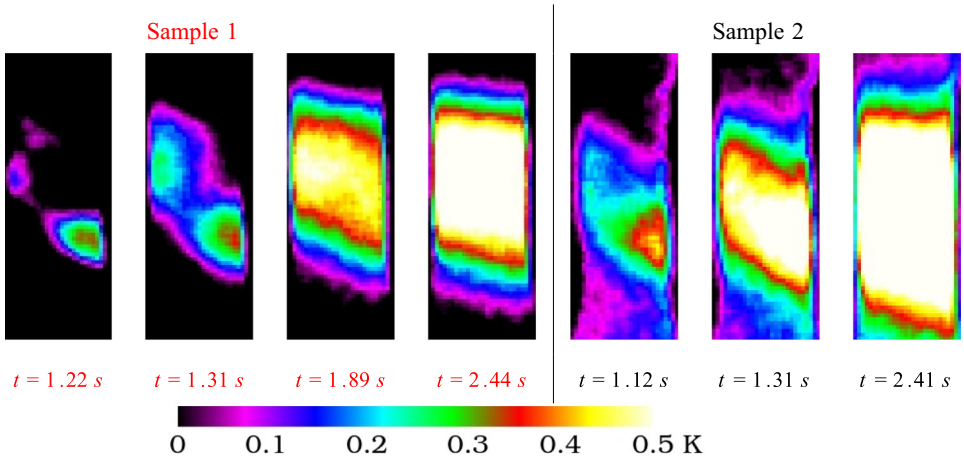

Fig. 5. Thermal fields of two tensile tests at room temperature and $\dot{\varepsilon} = 10^{-3}\ s^{-1}$. Sample 1 (left), sample 2 (right). Picture size: $9 \times 30\ mm^2$ corresponding to the gauge area (cf. Fig. 1(a)).

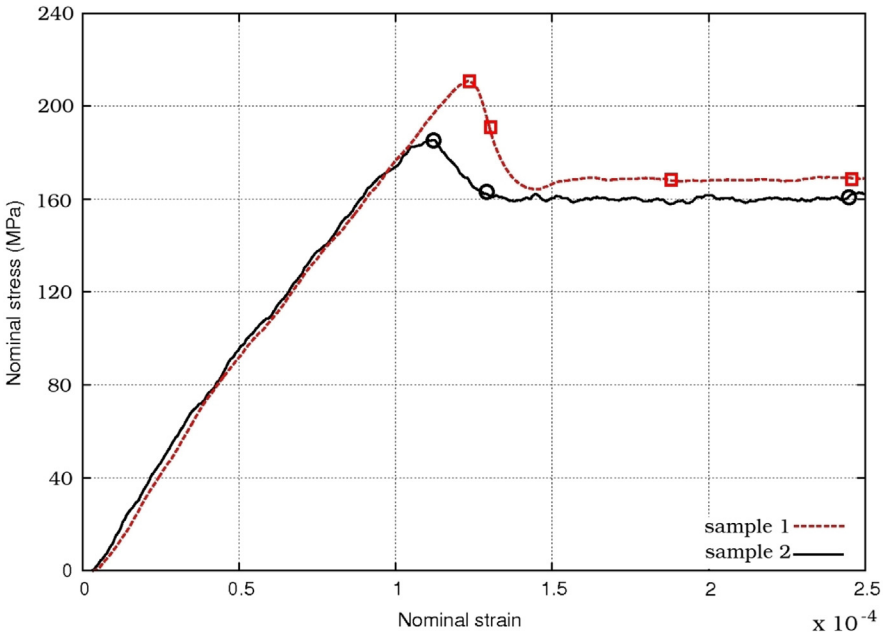

Fig. 6. Mechanical response of two tensile specimens at room temperature and $\dot{\varepsilon} = 10^{-3}\ s^{-1}$.

Similar observations have been done in the literature at the same scale in steels [23,44].

This interrupted tensile test has been carried out on a thin sample according to Fig. 1(a). Note that the same experiment has been done on the thick one (Fig. 1(b)), and no clear band propagation was observed neither at the macro scale nor at the micro-scale (no slip band at the surface).

3. Macroscopic aging model

The phenomenological elasto-viscoplastic model used in this work was first proposed by Penning [69] and then improved by Kubin–Estrin and McCormick (KEMC model) [56–60]. This model was originally designed to simulate the Portevin–Le Chatelier effect, but it is also suitable for Lüders band propagation [22]. It is based on the introduction of an internal variable t_a, representing the time during which solute atoms may diffuse along dislocations (mobile or forest) [70].

The KEMC model has been widely used, for many materials and applications [21,22,28,70–74]. It has been implemented in the finite element code *Zset* [79]. This model can be used for both static and dynamic strain aging, depending on the set of parameters chosen. In the case of static strain aging, t_a has a large initial value $t_{a\ 0}$ that represents the initial "pinned state". In this work this initial value is assumed to be equivalent to fully pinned, according to the aging experiments presented in Fig. 4.

3.1. Phenomenological model equations

The strain tensor is split into elastic and plastic contributions:

$$\tilde{\varepsilon} = \tilde{\varepsilon}_e + \tilde{\varepsilon}_p; \quad \tilde{\sigma} = \overline{\overline{E}} : \tilde{\varepsilon}_e \tag{1}$$

where $\overline{\overline{\bullet}}$ denotes a second order tensor, and $\tilde{\bullet}$ denotes a first order tensor.

A yield function is introduced:

$$f\,\tilde{\sigma} = J_2\left(\tilde{\sigma} - \sum_{i=1}^{2} \tilde{X}_i,\right) - R\rho - R_a(t_a) \tag{2}$$

with $J_2(\tilde{\sigma})$ being the von Mises equivalent to the stress.

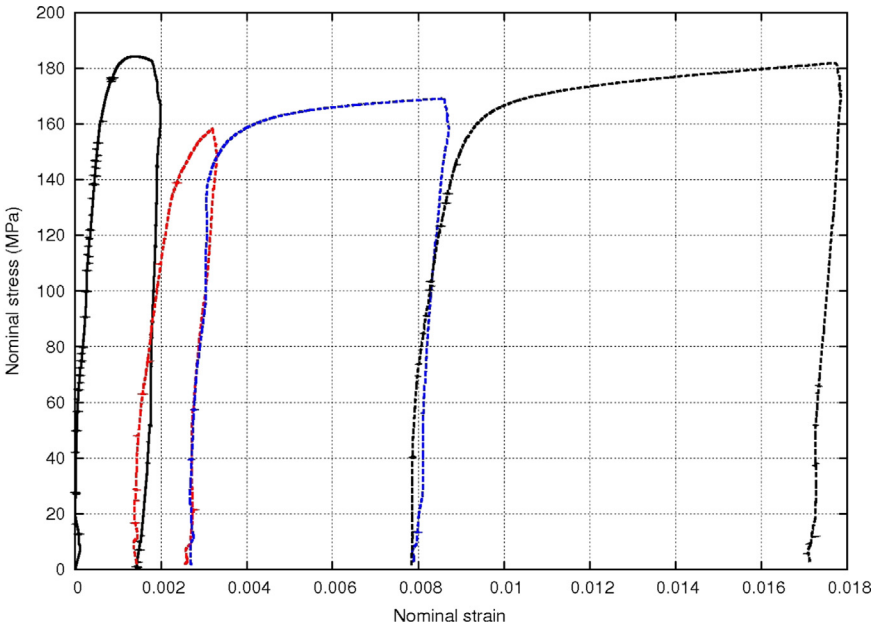

Fig. 7. Interrupted tensile test at $\approx 0.15\%$, $\approx 0.25\%$, $\approx 0.8\%$ and $\approx 1.7\%$ of macroscopic plastic strain.

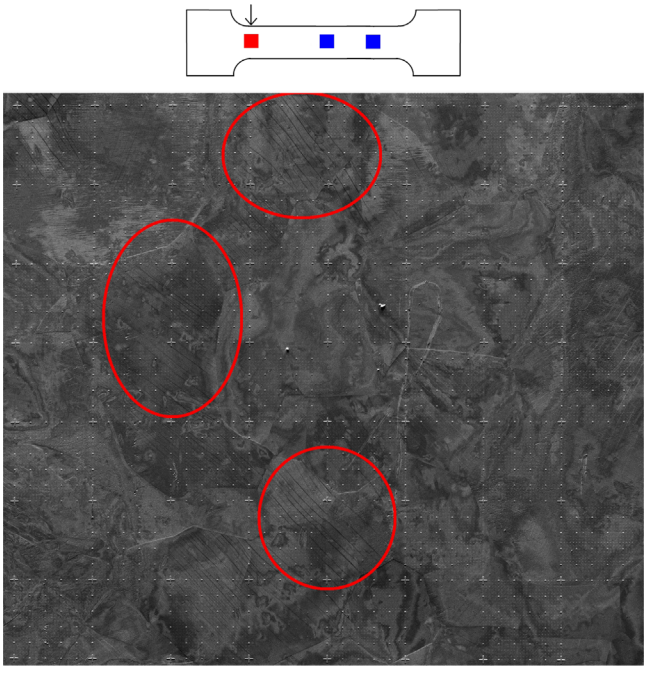

Fig. 8. SEM image of the $350 \times 400\ \mu m^2$ area near the left grip of the sample at $\approx 0.15\%$ of macroscopic plastic strain. The tensile direction corresponds to the horizontal direction. Red squares indicate the presence of slip lines, blue ones other areas without bands. The arrow indicates the position of the front band. (For interpretation of the references to color in this figure caption, the reader is referred to the web version of this paper.)

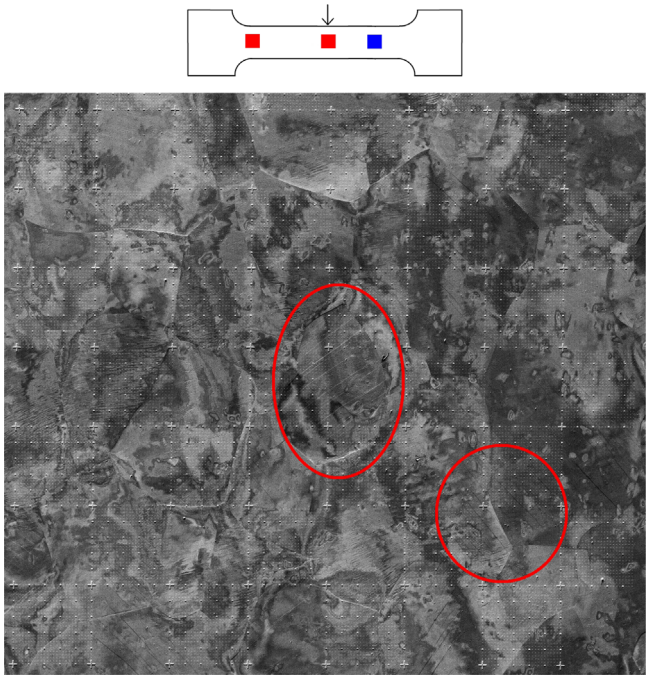

Fig. 9. SEM image of the $350 \times 400\ \mu m^2$ area in the center zone at $\approx 0.25\%$ of macroscopic plastic strain. The tensile direction corresponds to the horizontal direction. Red squares indicate the presence of slip lines, blue ones other areas without bands. The arrow indicates the position of the front band. (For interpretation of the references to color in this figure caption, the reader is referred to the web version of this paper.)

A non-linear kinematic hardening law is adopted [77,80]:

$$\vec{X}_i = \frac{2}{3} C_i \vec{\alpha}_i \quad \text{with } \dot{\vec{\alpha}}_i = \dot{\vec{\varepsilon}}_p - D_i \dot{p} \vec{\alpha}_i \tag{3}$$

C_i and D_i are kinematic hardening parameters. In this study, two kinematic hardening variables are used for an accurate description of the hysteresis loop.

The isotropic strain hardening is given by the term $R(\rho)$ which follows the evolution law defined as

$$R(\rho) = \gamma \mu b \sqrt{\rho} + R_0 \tag{4}$$

$\gamma$is the interaction coefficient, μ is the shear modulus and b is the norm of the Burgers vector. The dislocation density ρ is introduced in the model with an initial value ρ_0. Dislocation density evolution rule is driven by the cumulative plastic strain rate $\dot{p}$ and is written

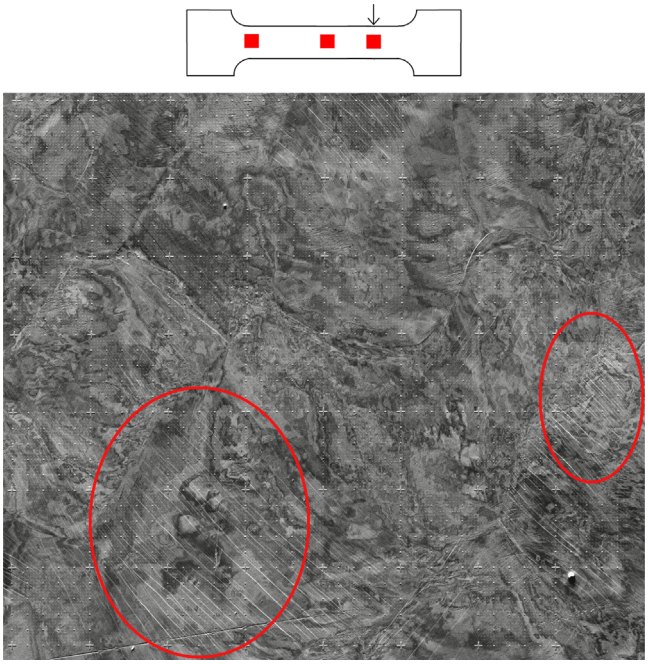

Fig. 10. SEM image of the $350 \times 400\ \mu m^2$ area near the right grip of the sample at $\approx 0.8\%$ of macroscopic plastic strain. The tensile direction corresponds to the horizontal direction. Red squares indicate the presence of slip lines, blue ones other areas without bands. The arrow indicates the position of the front band. (For interpretation of the references to color in this figure caption, the reader is referred to the web version of this paper.)

Table 2
KEMC model parameters identified for tantalum.

E	185,000 MPa	C_1	360×10^3 MPa	ρ_0	$10^{13}\ m^{-2}$
ν	0.3	D_1	3100	P_1	70 MPa
γ	0.13	C_2	550 MPa	P_2	$0.005\ s^{-\beta}$
R_0	2 MPa	D_2	2	β	0.66
A	$3 \times 10^{13}\ m^{-2}$	$\dot{p}_0$	$5 \times 10^{-5}\ s^{-1}$	ω	4×10^{-4}
B	$5 \times 10^{15}\ m^{-2}$	σ_0	14 MPa	$t_{a\,0}$	5×10^4 s

as the difference between a creation and an annihilation term:

$$\dot{\rho} = A\left[1 - \frac{\rho}{B}\right]\dot{p} \tag{5}$$

where A and B are two material parameters.

Strain aging induces an additional contribution to the yield stress:

$$R_a(t_a) = P_1 C_s(t_a) = P_1[1 - \exp(-P_2 t_a^{\beta})] \tag{6}$$

where C_s represents the over-concentration of solute atoms around pinned dislocations compared to equilibrium concentration. This variable increases with the aging time t_a, the totally pinned state being given by $C_s = 1$. The unpinned state corresponds to $C_s = 0$. The maximal additional stress required to unpin dislocations is driven by the parameter P_1. It can be related to the interaction force between mobile dislocations and solute atoms. P_2 and β control the kinetics of the pinning/unpinning process. Another parameter ω appears in the evolution law of the aging time and is related to the incremental strain resulting from the jump of unpinned dislocations. This parameter is kept constant here.

The aging time increment $\dot{t}_a$ is computed from an evolution law depending on the plastic strain rate $\dot{p}$:

$$\dot{t}_a = 1 - \frac{t_a}{t_w} \quad \text{with } t_w = \frac{\omega}{\dot{p}} \text{ and } t_a(t=0) = t_{a0} \tag{7}$$

t_w is defined as the waiting time of dislocations at obstacles and is related to the plastic strain rate $\dot{p}$.

The plastic strain is computed from the normality law rule and the equivalent plastic strain rate $\dot{p}$ follows an hyperbolic flow rule:

$$\dot{\bar{\varepsilon}}_p = \dot{p}\frac{\partial f}{\partial \tilde{\sigma}} \quad \text{with } \dot{p} = \dot{p}_0 \sinh\left\langle \frac{f(\tilde{\sigma})}{\sigma_0} \right\rangle \text{ where } \langle \bullet \rangle = \mathrm{Max}(\bullet, 0) \tag{8}$$

3.2. Identification of material parameters

The material parameters of the model were identified using the tensile tests at different strain rates, and a cyclic experiment at $\pm 0.2\%$. The identified parameters are given in Table 2. For the identification, homogeneous deformation was assumed. Thus, the parameters are identified by comparing experimental and simulation results based on standard optimization procedures [77].

Some parameters in Table 2 stem from the literature on tantalum. For instance, the parameter driving the yield stress is set to $\gamma = 0.13$ after [5]. The initial dislocation density $\rho_0 = 10^{13}\ m^{-2}$ is adopted from [5,14,61]. Moreover, the exponent β of the aging time stems from [75]. The initial value of the aging time $t_{a\,0}$ is set in order to ensure a sufficiently large initial pinning state, in our case $t_{a0} = 5 \times 10^4$ s, following [21]. At the beginning of simulation, R_a is close to P_1. As soon as plastic strain occurs, t_a and then $R_a(t_a)$ start decreasing to the final value $R_a(t_w)$ due to Eq. (7) which leads to the stress drop observed in Fig. 11.

Two kinematic hardening components were identified, for a better description of the hysteresis loops. Due to the very small cyclic hardening for strain amplitudes close to ± 0.2–0.25%, the isotropic hardening term turns out to be almost negligible.

The parameter $\omega = 4 \times 10^{-4}$ is set according to the literature [21,28,72]. $P_1 = 70$ MPa controls the aging contribution to the yield stress and therefore the maximum stress drop amplitude. $P_2 = 0.005\ s^{-\beta}$ controls the final value of $R_a(p, t_a)$ and is set in order to ensure a small contribution R_a when the unpinning process is achieved since t_a starts from $t_{a\,0}$ and tends to t_w according to Eq. (7).

The macroscopic stress–strain curves are plotted in Fig. 11 and are in good agreement with experiments. Tantalum exhibits a high strain rate sensitivity and a strong temperature dependence, whereas its work-hardening rate is relatively insensitive to these parameters. The strong Bauschinger effect is well captured by the model. There is only limited cyclic hardening for small strain amplitudes, which is in good agreement with experiment. However, the influence of the strain amplitude on the cyclic hardening (cf. Fig. 3) is not taken into account by the model.

3.3. Simulation on a full specimen

The previous identification strategy does not require any finite element simulation on the whole sample. However, finite element simulations are mandatory to validate the ability of the model to capture the main features of the strain localization phenomena associated (or not) to the anomalous yield point and its interaction with the viscosity. Thus, several simulations on full 3D specimens have been carried out using the FE code *Zset*. The mesh is built up from 20-nodes brick elements. Simulations have been performed using a total number of 7096 elements and 99,171 DOFs, with 4 elements in the sample thickness.

The fields of plastic strain and plastic strain rate are shown in Fig. 12 for 4 macroscopic strain levels defined in Fig. 13. They remain homogeneous over the gauge length during the tensile test simulation. The absence of band initiation and propagation, which is characteristic of other materials such as steels, results from the regularization effect of viscosity on strain localization [77]. The significant positive strain rate sensitivity of tantalum at room

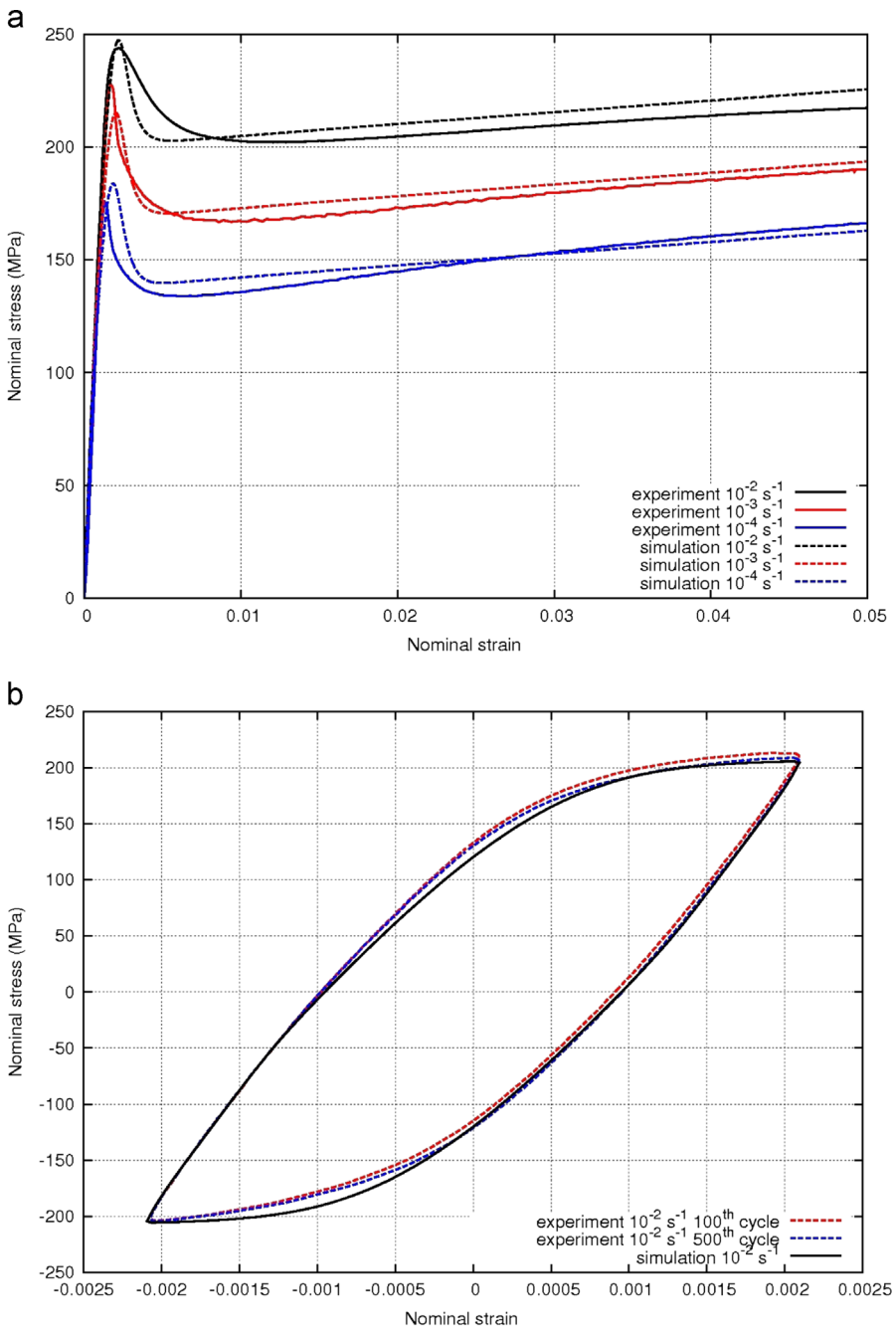

Fig. 11. (a) Tensile and (b) cyclic simulations at room temperature for $\dot{\varepsilon} = 10^{-4}\ s^{-1}$ to $\dot{\varepsilon} = 10^{-2}\ s^{-1}$. Comparison of the model with experiment.

temperature prevents plastic strain to localize in a deformation band in spite of the softening induced by unpinning.

4. Discussion

4.1. Impact of sample's misalignment on strain localization

Experimentally, it has been observed in Section 2 that a localization band can initiate and propagate through the sample. The previous simulation on a 3D specimen does not show such a localization pattern (Fig. 12). In order to understand the underlying phenomena driving the band occurrence, some perturbations of the FE simulations have been numerically tested.

Small perturbations in the experimental adjustments can change drastically the localization behavior, while the macroscopic response remains almost unchanged. A small misalignment of the upper grip has been applied, representing a slight change in the experimental setup. The main results are presented in Fig. 14. Boundary conditions consist of a prescribed vertical displacement of the upper grip coupled with a small horizontal head displacement at the first time step. Two different values for the misalignment have been tested: 200 μm and 500 μm. Such a small displacement has already been used to trigger Lüders bands in steels [21].

Fig. 13 shows the corresponding overall stress–strain curves. Four maps were selected at different loading stages as indicated by the number 1–4 in Fig. 13. The first map was chosen prior to the macroscopic stress maximum. We can notice in Fig. 14 for misaligned samples that plastic strain localization starts before the end of the macroscopic linear domain. This is in good agreement with experiment, for instance on IRT data. Moreover,

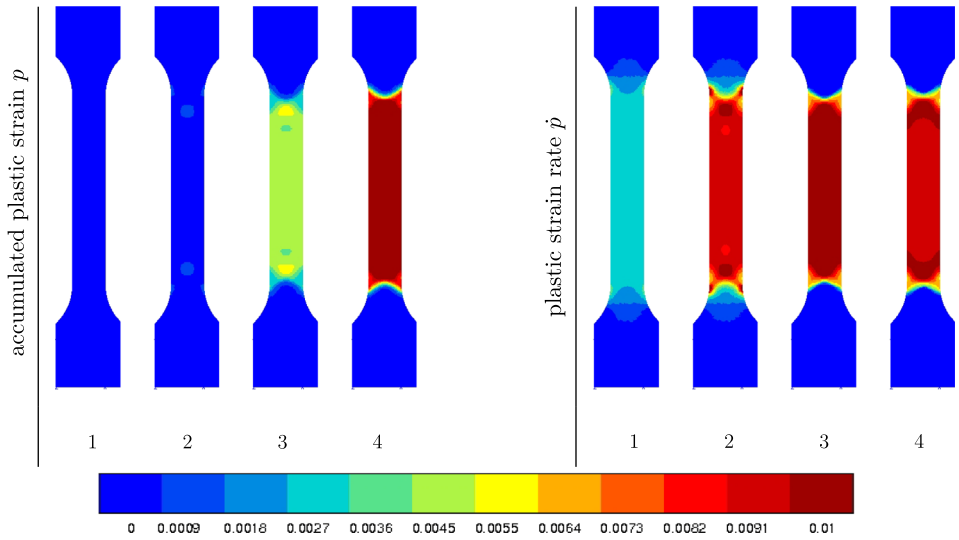

Fig. 12. Accumulated plastic strain (left) and plastic strain rates (right) during a tensile test at room temperature and $\dot{\varepsilon} = 10^{-3}\ s^{-1}$ of a 3D mesh for four different strain levels (1–4, cf. Fig. 13).

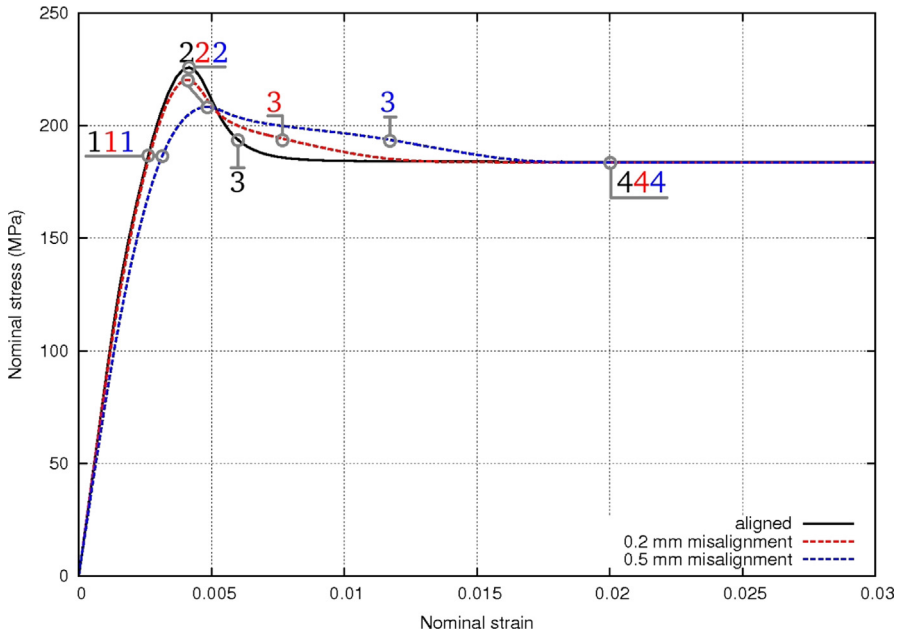

Fig. 13. Stress–strain curves of tensile test simulations at room temperature and $\dot{\varepsilon} = 10^{-3}\ s^{-1}$ of a 3D mesh for three different misalignments: aligned, 200 μm (or 0.4°) and 500 μm (or 1°) misalignment. Selected maps for Fig. 14 are indicated on the corresponding curves.

the microscopic yield stress of tantalum is set to 50 MPa in the literature [43]. When the misalignment of the upper grip increases, the strain localization becomes more pronounced. The localization band starts from one grip of the specimen and propagate simultaneously and symmetrically through the gauge width.

The localization band reaches the other side of the gauge width (map 2) at the macroscopic maximum stress. During the macroscopic stress softening, the localization band propagates along the sample (map 3). We can notice that the band front is more pronounced when the misalignment is set to 500 μm (or 1°), with a sharp strain gradient. Finally, map 4 corresponds to the beginning of hardening regime, where the strain and strain rate fields are homogeneous.

Moreover, we can notice that the shape of the macroscopic stress drop changes: when the misalignment increases, the stress drop becomes smaller and wider (cf. Fig. 13). The same observation has been done experimentally, for example on the IRT measurements: when the stress drop is smaller (sample 2), the band does not appear clearly on temperature field (Fig. 5). Thus, the non-systematic macroscopic occurrence of the localization bands associated to the anomalous yield point phenomenon can be due to some small experimental changes. If the sample is aligned, the strain rate sensitivity prevents plastic strain to localize. However, when a misalignment is imposed, the softening induced by unpinning leads to strain bands nucleation and propagation.

4.2. *Thermal field computation*

A post-processing of the temperature field during straining computation has been performed for the three samples in order to compare the thermal fields as predicted by the KEMC model with the experimental data from IRT. For the sake of simplicity, temperature changes are assumed to be induced by plastic

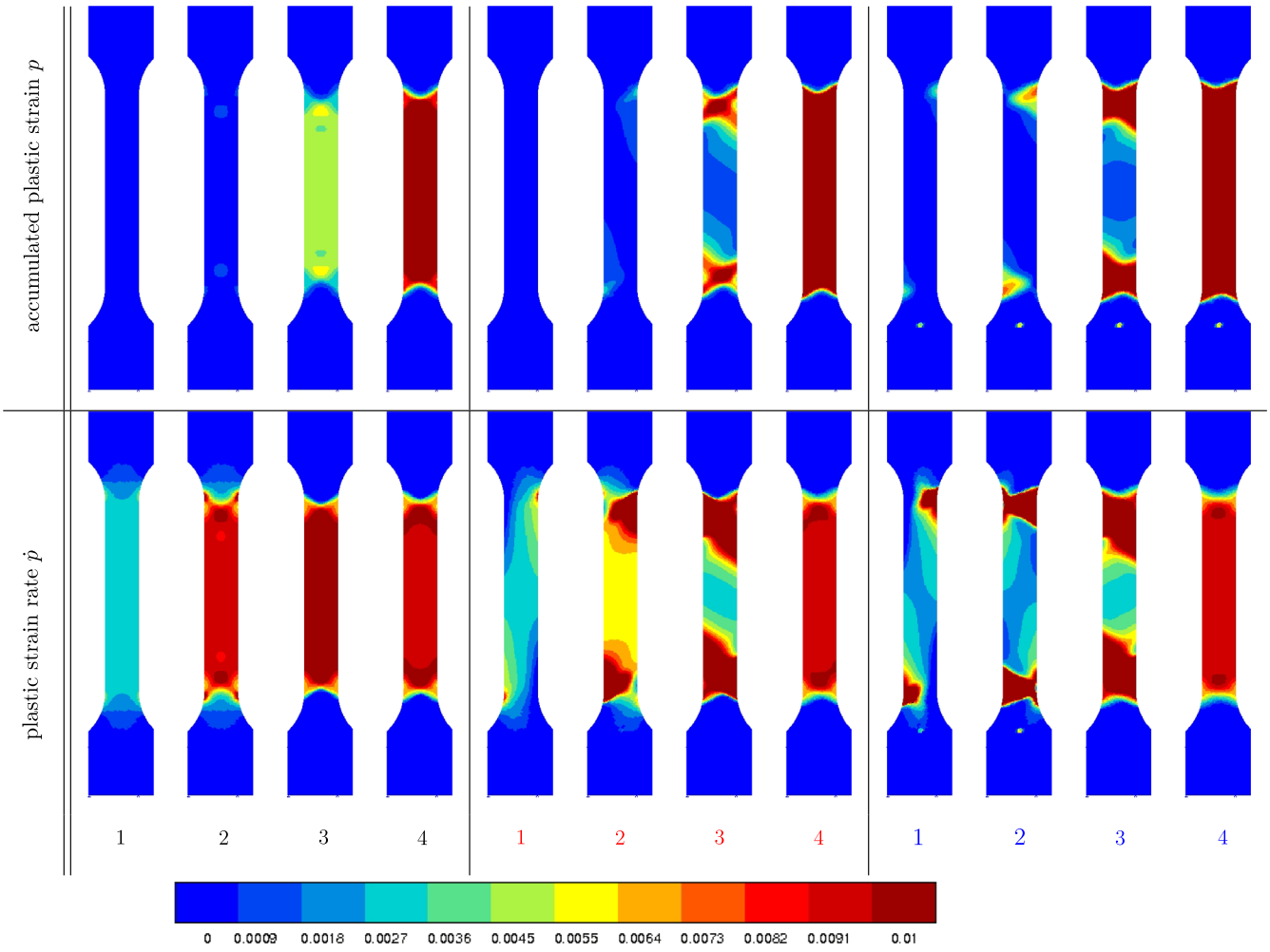

Fig. 14. Accumulated plastic strain (top) and plastic strain rate fields (bottom) during a tensile test at room temperature and $\dot{\varepsilon} = 10^{-3}\ s^{-1}$ of a 3D mesh for three different misalignments: aligned (left), 200 μm (center) misalignment (or 0.4°), 500 μm (right) misalignment (or 1°) and at four different strain levels (1 to 4) according to Fig. 13.

straining solely according to an adiabatic thermodynamic process. Thus, this post-processing is valid when conduction and convection terms are negligible.

The thermal field computation at the surface is based on the heat equation:

$$\rho\dot{\psi} + \rho\dot{T}s + \rho T\dot{s} = \tilde{\sigma} : \dot{\tilde{\varepsilon}} \tag{9}$$

with $\rho = 16.6 \times 10^3$ kg m^{-3} being the mass density of tantalum.

Using the Helmholtz free energy $\psi = e - Ts$ and neglecting the thermo-elastic coupling, Eq. (9) gives [80]:

$$\rho C\dot{T} = \tilde{\sigma} : \dot{\tilde{\varepsilon}}^{p} = \sigma_{eq}\dot{p} \quad \text{with } \rho\dot{e} = \rho C\dot{T} \tag{10}$$

with e being the internal energy density and $C = 0.14$ J g^{-1} K^{-1} being the heat capacity of tantalum.

Finally, the local heat increment associated to the plastic strain increment between two time-steps is computed using the following approximation:

$$T_{t+\Delta t} - T_t = \frac{\sigma_{eq(t+\Delta t)}}{\rho C}\Delta p \tag{11}$$

with σ_{eq} being the von Mises stress in each Gauss point between two time steps.

The predicted thermal fields using the KEMC model can be compared to those obtained by IRT (see Section 2.3). The misalignment effect on the thermal field has been tested and is presented in Fig. 15. Fig. 15 indicates that if the sample is aligned in the grips, the thermal field is homogeneous through the gauge length, leading to 1 K of overheating. If a slight misalignment is introduced, the maximal overheating remains rather small (< 1.5 K), but the thermal field is drastically modified: the strain localization associated to the stress drop leads to an heterogeneous thermal field. A localization band propagates along the gauge length, as observed experimentally by IRT (Fig. 6). However, the computation gives two bands nucleating near the grips where a single one nucleating in the center has been experimentally observed.

The amplitude of temperature change is in excellent agreement with the experimental results of Fig. 5. This result supports the hypothesis that the experimental setup may well be responsible for the presence or not of propagating band, and the variable shape of the stress drop.

5. Conclusion and outlook

Several mechanical tests have been carried out, pointing out the anomalous yield point phenomenon, a significant strain rate sensitivity, and the particular shape of the stress drop characteristic of pure tantalum.

Aging and strain reversal tests have been carried out, with a systematic anomalous yielding point if the aging time is sufficient (1 day at 100 °C). The results indicate that the anomalous yield point is due to strain aging, probably associated with the interaction of dislocations with oxygen atoms.

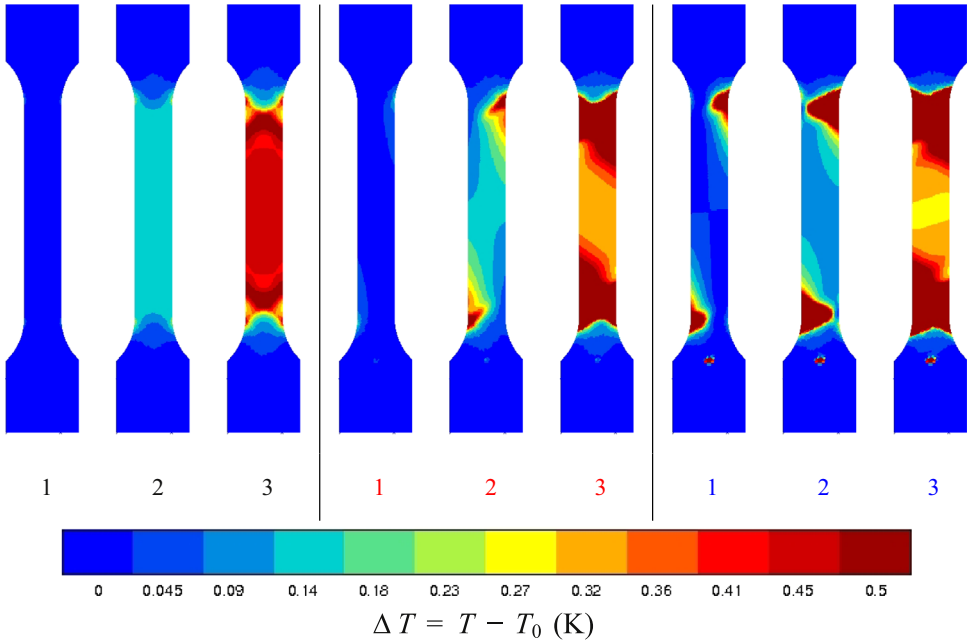

Fig. 15. Field of temperature increase during a tensile test at $\dot{\varepsilon} = 10^{-3}\ s^{-1}$ for three misalignment parameters: aligned (left), 200 μm of misalignment (center), 500 μm of misalignment (right) and for four strain values after Fig. 13.

The IRT measurements suggest that the anomalous yield point can be accompanied by the propagation of deformation band with slight strain localization. This fact is confirmed by SEM observations performed during an interrupted tensile test of noticeable slip lines at the surface in the region of a propagating band front. The specimen thickness seems to have a decisive influence on its appearance.

A macroscopic phenomenological KEMC model has been identified at room temperature for monotonic and cyclic loadings. The macroscopical response is in good agreement with experiments. Based on 3D FE simulation, it has been shown that a slight misalignment of the sample can lead to a drastic change of the localization pattern in the sample. A displacement of 200 μm (or 0.4°) is sufficient to trigger a strain localization band that nucleates at one grip and propagates through the gauge length. The heterogeneous thermal field associated to the band propagation is well captured by the model, using the adiabatic assumption. The conclusion is that the strong strain rate sensitivity of the material at room temperature significantly limits the Lüders-like behavior of tantalum even though huge strain drops are observed.

References

[1] R. Lachenmann, H. Schultz, Scr. Metall. 4 (1970) 709–714.
[2] S. Takeuchi, E. Kuramoto, T. Suzuki, Acta Metall. 20 (1972) 909–915.
[3] S. Takeuchi, K. Maeda, Acta Metall. 25 (1977) 1485–1490.
[4] A.E. Diaz, R.E. Reed-Hill, Scr. Metall. 13 (1979) 491–496.
[5] W. Wasserbach, Work-Hardening and Dislocation Behaviour of Tantalum and Tantalum Alloys, The Minerals, Metals and Materials Society, 1996.
[6] D. Rittel, M.L. Silva, B. Poon, G. Ravichandran, Mech. Mater. 41 (2009) 1323–1329.
[7] S. Nemat-Nasser, J.B. Isaacs, M. Liu, Acta Mater. 46 (1998) 1307–1325.
[8] S. Nemat-Nasser, T. Okinaka, L. Ni, J. Mech. Phys. Solids 46 (1998) 1009–1038.
[9] S.E. Schoenfeld, Int. J. Plast. 14 (1998) 871–890.
[10] Y.J. Chen, M.A. Meyers, V.F. Nesterenko, Mater. Sci. Eng. A 268 (1999) 70–82.
[11] F. Llorca, A. Juanicotena, C. Dambrun, Shock Compres. Condens. Mater. 505 (2000) 455–458.
[12] P.J. Maudlin, J.F. Bingert, G.T. Gray III, Int. J. Plast. 19 (2003) 483–515.
[13] C.A. Bronkhorst, E.K. Cerreta, Q. Xue, P.J. Maudlin, T.A. Mason, G.T. Gray III, Int. J. Plast. 22 (2006) 1304–1335.
[14] E. Hosseini, M. Kazeminezhad, Int. J. Refract. Metals Hard Mater. 27 (2009) 605–610.
[15] T.E. Mitchell, W.A. Spitzig, Acta Metall. 13 (1965) 1169–1179.
[16] B.L. Mordike, G. Rudolph, J. Mater. Sci. 2 (1967) 332–338.
[17] S.C. Park, Some aspects of dynamic strain aging in the niobium-oxygen system (Ph.D. thesis), University of Florida, 1983.
[18] M. Kothari, L. Anand, J. Mech. Phys. Solids 46 (1998) 51–83.
[19] R.L. Smialek, T.E. Mitchell, Philos. Mag. 22 (1970) 1105–1127.
[20] T.W. Barbee, R.A. Huggins, J. Less Common Metals 8 (1965) 306–319.
[21] A. Marais, M. Mazière, S. Forest, A. Parrot, P. Le Delliou, Philos. Mag. 92 (2012) 3589–3617.
[22] J. Belotteau, C. Berdin, S. Forest, A. Parrot, C. Prioul, Mater. Sci. Eng. A 526 (2009) 156–165.
[23] M. Soler, Etude du vieillissement d'un acier à bake-hardening: évolution des propriétés mécaniques de traction—corrélation de la microstructure (Ph.D. thesis), INSA Lyon, 1998.
[24] C. Sommer, H. Mughrabi, D. Lochner, Acta Mater. 46 (1998) 1527–1536.
[25] C. Sommer, H. Mughrabi, D. Lochner, Acta Mater. 46 (1998) 1537–1546.
[26] W. Lüders, Dinglers Polytech. J. 155 (1860) 18–22.
[27] J. Zhang, Y. Jiang, Int. J. Plast. 21 (2005) 651–670.
[28] S. Graff, S. Forest, J.L. Strudel, C. Prioul, P. Pilvin, J.L. Bechade, Mater. Sci. Eng. A 387–389 (2004) 181–185.
[29] S. Graff, S. Forest, J.L. Strudel, C. Prioul, P. Pilvin, J.L. Bechade, Scr. Mater. 52 (2005) 1181–1186.
[30] S. Graff, Viscoplastic behavior of zirconium alloys in the temperature range 20C–400C: characterization and modelling of strain ageing (Ph.D. thesis), Ecole Nationale Supérieure des Mines de Paris, 2006.
[31] W. Thorpe, I. Smith, J. Nucl. Mater. 78 (1978) 49–57.
[32] H. Jousset, L. Remy, J.L. Strudel, Prog. Mech. Behav. Mater. 2 (1999) 580–585.
[33] H. Jousset, Viscoplasticité et microstructures d'un alliage de titane: effets de la température et de la vitesse de sollicitation (Ph.D. thesis), Ecole Nationale Supérieure des Mines de Paris, 2008.
[34] H. Conrad, Prog. Mater. Sci. 26 (1981) 123–403.
[35] R.W. Powers, M.V. Doyle, Acta Metall. 4 (1956) 233–242.
[36] M. Weller, J.X. Zhang, G.Y. Li, T.S. Ke, J. Diehl, Acta Metall. 29 (1981) 1055–1060.
[37] A. Cottrell, B. Bilby, Proc. Phys. Soc. Conf. A 62 (1949) 49–62.
[38] P. Hirsch, 5th International Congress of Crystallography, Cambridge, 1960.
[39] B. Sestak, N. Zarubova, Phys. Status Solidi b 10 (1965) 239–250.
[40] F. Kroupa, Plastic deformation of BCC metals with special reference to slip geometry, Ecole d'été de Pont-à-Mousson, Nancy, 1967.
[41] V. Vitek, Cryst. Lattice Defects 5 (1974) 1–34.
[42] K.G. Hoge, A.K. Mukherjee, J. Mater. Sci. 12 (1977) 1666–1672.
[43] S. Frénois, Modélisation polycristalline du comportement mécanique du tantale. Application à la mise en forme par hydroformage (Ph.D. thesis), Centrale Paris, 2001.
[44] A. Nadai, Plasticity—A Mechanics of the Plastic State of Matter, Mc Grow-Hill Company, New York, 1931.
[45] Z.C. Szkopiak, W. Eliasz, J. Less Common Metals 11 (1966) 273–285.
[46] N.M. Fonshteyn, V.I. Sarrak, S.B. Maslenkov, Phys. Metals Metallogr. 14 (1969) 156.
[47] M.G. Ulitchny, R. Gibala, J. Less Common Metals 33 (1973) 105–116.
[48] A. Falanga, Influence des éléments interstitiels dans le tantale, Note interne CEA, 1979.

[49] K.S. Chan, J. Lankford, Acta Metall. 36 (1988) 193–206.
[50] T. Paris, Modélisation du comportement mécanique des liaisons soudées hétérogènes Ta/TA6V4 : comportement et critère de rupture (Ph.D. thesis), Université de Technologie de Troyes, 2008.
[51] S. Frenois, E. Munier, P. Pilvin, Adv. Mech. Behav. Plast. Damage (2000) 431–436.
[52] S. Frenois, E. Munier, X. Feaugas, P. Pilvin, J. Phys. IV 11 (2001) 301–308.
[53] F. Buy, Etude expérimentale et modélisation du comportement plastique du tantale. Prise en compte de la vitesse de déformation et de l'histoire de chargement (Ph.D. thesis), Université de Metz, 1996.
[54] T. Magnin, J. Driver, J.N. Lepinoux, L.P. Kubin, Rev. Phys. Appl. 19 (1984) 467–482.
[55] G. Piobert, Mémoire de l'Artillerie, 1842.
[56] L.P. Kubin, Y. Estrin, P. Spiesser, Res. Mech. 10 (1984) 25–38.
[57] L.P. Kubin, Y. Estrin, Acta Metall. 33 (1985) 397–407.
[58] L.P. Kubin, Y. Estrin, Scr. Metall. 23 (1989) 815–817.
[59] L.P. Kubin, Y. Estrin, Acta Metall. 38-5 (1989) 697–708.
[60] P. McCormick, Acta Metall. 36 (1998) 3061–3067.
[61] M.N. Norlain, Comportement mécanique du tantale, texture et recristallisation (Ph.D. thesis), Travaux non-publiés, 1999.
[62] C. Kerisit, Analyse de recristallisation statique du tantale déformé á froid pour une modélisation en champ moyen (Ph.D. thesis), Ecole Nationale Supérieure de Mines de Paris, 2012.
[63] A. Chrysochoos, H. Louche, Int. J. Eng. Sci. 38 (2000) 1759–1788.
[64] H. Louche, A. Chrysochoos, Mater. Sci. Eng. A 307 (2001) 15–22.
[65] A. Chrysochoos, Proc. IUTAM 4 (2012) 15–26.
[66] H. Mughrabi, K. Herz, X. Stark, Int. J. Fract. 17 (1981) 193–220.
[67] K. Takao, K. Kusukawa, Mater. Sci. Eng. A 213 (1996) 81–85.
[68] R.A. Elliot, E. Orowan, T. Udoguchi, A.S. Argon, Mech. Mater. 36 (2004) 1143–1153.
[69] P. Penning, Acta Metall. 20 (1972) 1169–1175.
[70] S. Zhang, P. McCormick, Y. Estrin, Acta Mater. 49 (2000) 1087–1094.
[71] M. Mazière, J. Besson, S. Forest, B. Tanguy, H. Chalons, F. Vogel, Comput. Methods Appl. Mech. Eng. 199 (2010) 734–754.
[72] H.D. Wang, C. Berdin, M. Mazière, S. Forest, C. Prioul, A. Parrot, P. Le-Delliou, Scr. Mater. 64 (2011) 430–433.
[73] M. Mazière, H. Dierke, Comput. Mater. Sci. 52 (2012) 68–72.
[74] J.-L. Chaboche, A. Gaubert, P. Kanouté, A. Longuet, F. Azzouz, M. Mazière, Int. J. Plast. 46 (2013) 1–22.
[75] J. Friedel, Dislocations, Pergamon Press, New York, 1964.
[76] G. Saada, T. Kruml, Philos. Mag. 93 (2013) 256–271.
[77] J. Besson, J.G. Cailletaud, J.-L. Chaboche, S. Forest. Mécanique non linéaire des matériaux, Hermès Science, 2001.
[78] L. Blanc., J.-L. Strudel, Dynamic strain ageing and relaxation in 316L type stainless steel, in: Proceedings of the 7th International Conference on the Strength of Metal and Alloys, 1985.
[79] Zset Software, ⟨http://www.zset-software.com⟩.
[80] J.L. Chaboche, J.J. Lemaitre, Mécanique des matériaux solides. Ed. 3. Dunod.